Development of the SJTU Unfoldable Robotic System (SURS) for Single Port Laparoscopy

Kai Xu, *Member, IEEE*, Jiangran Zhao, *Student Member, IEEE*, and Minxiao Fu

***Abstract*—Single-port laparoscopy (SPL) has attracted continuous attention in the past decade due to the potential of generating better surgical outcomes than the traditional multiport laparoscopy. In order to ease the challenging surgical manipulation tasks using manual tools in SPL, several robotic systems were constructed to provide surgeons an intuitive way to operate. With possible improvements identified, the SJTU unfoldable robotic system (SURS) for SPL is developed for improved system specifications. The SURS can be deployed into abdomen through a ϕ12-mm port in its folded configuration and can then be unfolded for dual-arm surgical interventions with onboard 3-D visual guidance. A few key design concepts which lead to the specification improvements are elaborated. The design descriptions, kinematics modeling, actuation compensations, and experimental characterizations are detailed to demonstrate the potentials of the SURS.**

***Index Terms*—Actuation compensation, continuum mechanism, kinematics, single-port laparoscopy (SPL), surgical robot.**

I. Introduction

SINGLE-PORT laparoscopy (SPL) has attracted continuous attention in the past decade due to the potential of generating better surgical outcomes than the traditional multiport laparoscopy [1]. Although newly developed surgical instruments have enabled manual SPL operations, it is still very challenging for surgeons to perform SPL procedures due to the crossed and mirrored hand–eye coordination. Surgeons might have to go through substantial training sessions to familiarize themselves with these new tools, such as the Novare RealHand tools, the CambridgeEndo Laparo-Angle instruments, the SPIDER device, the SILS port from Covidien, the TriPort, and QuadPort from Advanced Surgical Concepts, etc.

In order to address the manipulation difficulties in SPL, several robotic systems and mechatronic devices were designed and constructed to provide surgeons an intuitive way to operate in SPL. The existing state of the art is reviewed in Section II as benchmarking references for the design objectives of this effort to develop a new SPL robot. Besides the devices and systems dedicated to SPL procedures, the review in Section II also covers the robotic systems designed for natural orifice translumenal endoscopic surgery (NOTES) procedures. These NOTES robots all could be delivered to surgical sites through a natural orifice (e.g., GI tract, vagina, etc.) using an endoscope. Their system specifications were taken into consideration when design objectives were determined for this presented design.

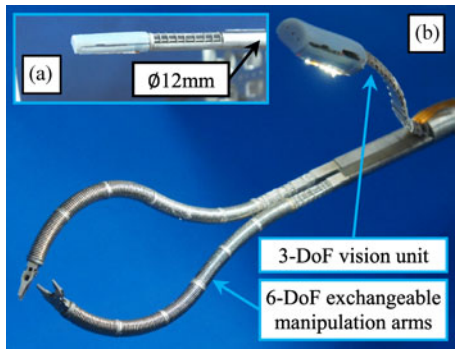

Fig. 1. Constructed SURS robot: (a) folded configuration deployable through a ϕ12-mm incision, (b) unfolded working configuration.

Examining the existing robots for SPL and NOTES, a few performance improvements could still be identified: 1) the diameter of the access port could be further reduced; 2) the workspace and the payload capabilities of the inserted manipulation arms could be further tuned; and 3) maintainability and modularity could be improved. Trying to achieve improved system specifications and push the design boundaries of a SPL robot, the SJTU unfoldable robotic system (SURS) is developed as shown in Fig. 1. It can be deployed into abdomen through a ϕ12-mm port in its folded configuration and can then be unfolded into a dual-arm configuration for surgical tasks. It possesses 15 degrees of freedom (DoFs), including one 3-DoF vision unit and two 6-DoF manipulation arms.

Major contributions of this paper include a few key design concepts as presented in Section III. They could also be applied to other instrument or manipulator designs, besides the specific embodiments in Section IV. Minor contributions include a modified actuation compensation procedure for improving the motion accuracy of the SURS's manipulation arms.

This paper is organized as follows. Section II reviews the existing state-of-the-art systems for SPL and NOTES, as well as summarizes the design objectives of the SURS. With the overview and the design concepts presented in Section III, Section IV describes the system components in detail. Section V presents the kinematics of the SURS's manipulation arms. Various experimental characterizations, including actuation compensation, of the SURS are presented in Section VI, with conclusions summarized in Section VII.

Manuscript received June 24, 2014; revised August 25, 2014; accepted October 15, 2014. Recommended by Technical Editor Prof. D. Stoianovici. This work was supported in part by the Global Research Outreach program of the Samsung Advanced Institute of Technology, in part by the National Natural Science Foundation of China under Grant 51375295, and in part by the Shanghai Rising-Star Program under Grant 14QA1402100.

The authors are with the Lab of Robotics Innovation and Intervention, University of Michigan–Shanghai Jiao Tong University Joint Institute, Shanghai Jiao Tong University, Shanghai 200240, China (e-mail: k.xu@sjtu.edu.cn; zjr318@sjtu.edu.cn; fuminxiao@sjtu.edu.cn).

Color versions of one or more of the figures in this paper are available online at http://ieeexplore.ieee.org.

Digital Object Identifier 10.1109/TMECH.2014.2364625

II. Existing State of the Art and Design Objectives

Surgical robots for SPL and/or NOTES share many similar characteristics. Most of them possess a common configuration of one vision unit and two manipulation arms. All of the system components can be deployed through a single channel (a laparoscopic access port or an endoscope) to surgical sites. Several robotic systems have been developed in order to facilitate SPL and/or NOTES procedures.

The SPL robot with two 5-DoF arms developed by Sekiguchi *et al.* [2] can be deployed into abdomen through a ϕ30-mm trocar. An updated version has two 6-DoF arms and uses a ϕ25-mm incision [3]. Lee *et al.* developed an SPL robot using stackable four-bar linkages [4], where two 5-DoF arms can be deployed through a ϕ25-mm port. Titan Medical Inc. announced its Single Port Orifice Robotic Technology (SPORT) surgical system [5]. The system could also be deployed through a ϕ25-mm incision, whereas each arm has 8-DoFs with a payload capability of around 3.25 N. Picciagallo *et al.* [6] constructed the SPRINT robot for SPL. The robot with two 6-DoF arms and an outer diameter of ϕ23-mm has a payload capability of 5 N. A modified version is reported in [7] with two 6-DoF arms using a ϕ30-mm access port. Shin and Kwon developed a 6-DoF ϕ8-mm manipulator for SPL with a payload capability of more than 7.5 N [8]. A ϕ16-mm port might be needed to form a dual-arm configuration. Ding *et al.* developed the IREP robots for SPL [9], [10]. It possesses two 7-DoF arms and can be deployed through a ϕ15-mm port. Intuitive Surgical Inc. introduced the VeSPA instrument to be used with the da Vinci robot [11]. The typical setup involves the use of a ϕ35-mm port. The da Vinci SP system was also released recently: it has three 7-DoF arms and uses a ϕ25-mm access port [12]. Besides the SPL robotic systems, several imaging systems for SPL were also developed [13]–[17].

Besides the SPL robots, a number of NOTES robots were also developed. Phee *et al.* presented a ϕ22-mm dual-arm robot [18]. Each arm has 4-DoFs and a payload capability of 3 N. Abbott *et al.* developed the ViaCath system for NOTES [19]. It needs a ϕ19-mm port but the instrument's payload is only 0.5 N. Lehman *et al.* developed an articulated NOTES robot, which can be magnetically anchored to abdominal wall [20]. The robot has a cross section of 14×17 mm and two 3-DoF arms. Harada *et al.* introduced a reconfigurable modular robot for NOTES with an outer diameter of 15.4 mm [21]. The design has evolved into a more compact and completed version as in [22] and [23]. The latest version with different ϕ12-mm modules could be reconfigured to form two 4-DoF arms with a payload capability of 0.65 N. Zhao *et al.* developed a testbed to characterize enabling features for NOTES [24]. One vision unit and two 5-DoF arms with a payload capability of 2 N could be housed in a ϕ12-mm endoscope.

The summary of the existing state-of-the-art SPL and NOTES robots can be found in Table I.

A key specification of a SPL/NOTES robot could be the diameter of the access port if other specifications (e.g., the number of DoFs, workspace, and payload capabilities) are comparable. It can be seen from Table I that the existing NOTES robots are generally constrained to a smaller diameter to ensure their passage through curved natural orifices. On the other side, the existing SPL robots usually possess two arms with bigger numbers of DoFs and higher payload capabilities. Then, it might be an ideal case to let an SPL surgical robot have both: the robot can be deployed through a small skin incision but still possesses big workspace, enhanced distal dexterity and high payload capabilities.

TABLE I
Existing State-of-the-Art SPL/NOTES Robots

Procedure	System or developer	Port size (mm)	Arm DoFs	Payload
SPL	Sekiguchi *et al.* [2]	ϕ30	5	-
SPL	Kobayashi *et al.* [3]	ϕ25	6	
SPL	Lee, Choi and Yi [4]	ϕ25	5	-
SPL	The SPORT system [5]	ϕ25	8	$>$ 3.25 N
SPL	The SPRINT robot [6]	ϕ23	6	5 N
SPL	The new SPRINT robot [7]	ϕ30	6	-
SPL	Shin and Kwon [8]	$>\phi$16	6	$>$ 7.5 N
SPL	The IREP robot [9], [10]	ϕ15	7	-
SPL	The VeSPA instruments [11]	ϕ35	-	-
SPL	The da Vinci SP system [12]	ϕ25	7	
NOTES	Phee *et al.* [18]	ϕ22	4	3 N
NOTES	The ViaCath system [19]	ϕ19	6	0.5 N
NOTES	Lehman *et al.* [20]	14×17	3	-
NOTES	Harada *et al.* [21]	ϕ15.4	-	-
NOTES	Tortora *et al.* [22], [23]	ϕ12	4	0.65 N
NOTES	Zhao *et al.* [24]	ϕ12	5	2 N

Toward the aforementioned ideal design goals, this effort aims at achieving improved specifications of a SPL robot. The design objectives were hence determined as follows.

1) The SURS should only use a ϕ12-mm access port. Since the IREP robot for SPL needs a ϕ15-mm access port [9], [10], it is better to aim at a smaller diameter.
2) It should possess two 6-DoF manipulation arms to ensure adequate workspace and fair distal dexterity.
3) Each arm shall have a payload capability of 2 N. The threshold forces to maintain fully articulated states of the RealHand tools and the Laparo-Angle instruments are 1.6 N and 1.8 N, respectively [25]. The design goal is set to 2 N because these clinically applied manual tools generate comparable forces. It should be noted that this payload capability does not guarantee the completion of an arbitrary surgical task (e.g., retraction is not possible with low forces).
4) Actuation modularity shall be enhanced. The manipulation arms with different end effectors (e.g., grippers, needle drivers, ablation tips) could be easily replaced during a surgery. Sterilization of these arms should be considered.
5) A 3-D vision unit with illumination should be included.

III. System Overview and Design Concepts

Following the design objectives outlined in Section II, the SURS was constructed as in Figs. 1 and 2. Its base plate could be attached to a conventional 6R industrial robot. The 6R industrial robot serves as the remote center of motion (RCM) mechanism

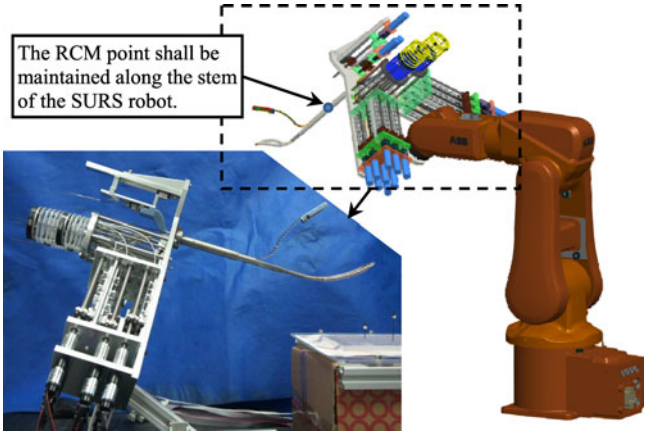

Fig. 2. Setup overview of the SURS attached to an industrial robot.

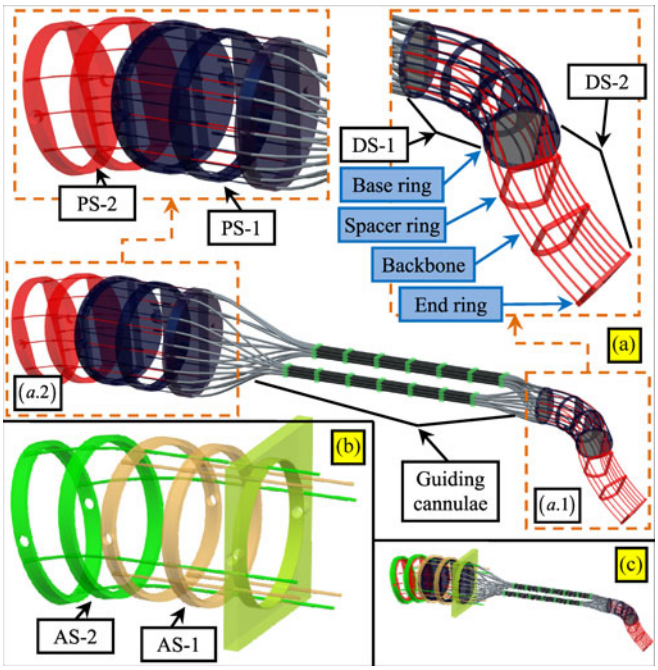

Fig. 3. (a) Dual continuum mechanism, (b) actuation structure, and (c) dual mechanism assembled into the actuation structure: DS, PS, and AS stand for the distal segment, the proximal segment and the actuation segment, respectively.

and provides rough positioning of the SURS about the incision point in the abdominal wall.

As shown in Fig. 1, the SURS could be folded into a ϕ12-mm cylindrical form (a stem), and positioned by the industrial robot for insertion through a skin incision into the abdomen. It then unfolds itself into a dual-arm working configuration. Two major design concepts were implemented in order to meet the demanding design objectives outlined in Section II.

A. Dual Continuum Mechanism With Actuation Modularity

The first design concept is a dual continuum mechanism as shown in Fig. 3(a). It consists of a multisegment distal structure, a multisegment proximal structure, and a set of rigid guiding cannulae.

1) The distal structure as in Fig. 3(a.1) consists of the distal segment 1 (DS-1) and the distal segment 2 (DS-2).
2) The proximal structure consists of the proximal segment 1 (PS-1) and the proximal segment 2 (PS-2) as in Fig. 3(a.2).
3) A segment is also depicted in Fig. 11 and it consists of a base ring, several spacer rings, an end ring, and several backbones. These rings could have circular or arbitrary shapes.
4) The backbones are thin rods made from nitinol (superelastic nickel titanium alloy) and could be both pulled and pushed. This extends the definition of a backbone from that in [26].

For each segment, the backbones are all attached to the end ring and can slide in the holes in the spacer rings and in the base ring. Three DoFs of each segment could be realized by simultaneous push–pull actuation of the backbones: 1) a 2-DoF bending by differential push–pull actuation and 2) a 1-DoF extension/compression by synchronized push–pull actuation. The spacer rings shall be evenly distributed as to prevent buckling of the backbones when they are pushed.

The DS-1 and the PS-1 are connected: the DS-1's backbones are attached to the DS-1's end ring, and routed through the DS-1, the rigid guiding cannulae, the PS-1, and attached to the PS-1's end ring. The arrangement of the backbones in the DS-1 is similar and scaled to that in the PS-1. Hence, the PS-1's bending would bend the DS-1 in the opposite direction; shortening the PS-1 would extend the DS-1 and vice versa.

The DS-2 could be serially stacked to the DS-1 so that the distal structure would possess more DoFs. Then, the DS-2's backbones are routed through the DS-1, the guiding cannulae, the PS-1 and attached to the PS-2's end ring. Actuation of the PS-2 would drive the DS-2 accordingly.

Fig. 3(b) shows a multisegment actuation structure, which consists of the actuation segment 1 (AS-1) and the actuation segment 2 (AS-2). Each segment in the structure has four actuation backbones. Push–pull actuation of the backbones would bend, extend, or compress the corresponding segments.

The proximal structure of the dual continuum mechanism could be assembled into the actuation structure as shown in Fig. 3(c) so that the AS-1 and the AS-2 bend, or extend/compress the PS-1 and the PS-2 so as to drive the DS-1 and the DS-2 accordingly, no matter how many backbones are arranged in the distal continuum structure.

As in Fig. 3(a), the guiding cannulae could be bounded arbitrarily and their arrangement does not have to be similar to those of the backbones. As long as the cannulae remain rigid and provide smooth channels to pass through the backbones, actuation of the distal structure will not be affected. This is a critical feature of the dual continuum mechanism, which allows the outer diameter of the SURS to be reduced to 12 mm.

This dual continuum mechanism also introduces actuation modularity. The segments in the distal structures could be designed for different lengths, different sizes, and/or with different end effectors attached. As long as the same proximal structure is used, one actuation structure would be able to drive all the

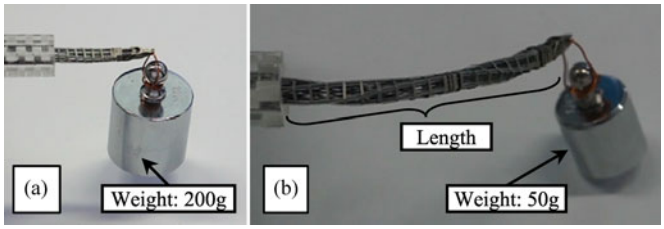

Fig. 4. Torsional stability of a continuum manipulator affects the payload capability: (a) shortened manipulator lifted 200 g, and (b) extended manipulator failed to lift 50 g.

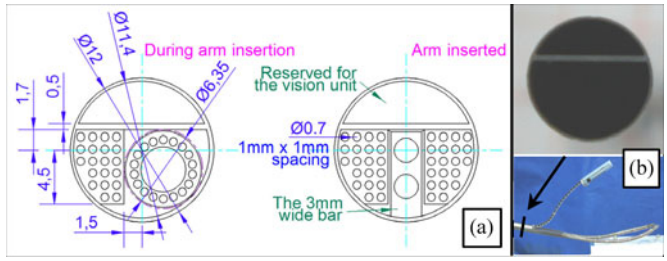

Fig. 5. Layout of the stem cross section: (a) CAD model and (b) prototype.

different distal structures. The only modification needed is to change to corresponding actuation parameters in the controller for these different distal structures. What is more, the dual continuum mechanism is a pure mechanical structure. While disassembled from the actuation structure, sterilization could be easily performed.

B. Payload Capability Enhancement

The dual continuum mechanism has inherent flexibility. In order to enhance its payload capability, an immediate solution might be to increase the number of the backbones. Due to the actuation modularity, the dual continuum mechanism could be actuated consistently no matter how many backbones are used.

However, increasing the number of backbones is not a complete solution. In the weight lifting experiments using the testbed system as in [24], torsional stability of a continuum manipulator greatly affects the payload capability. As shown in Fig. 4, a shortened manipulator could lift 200 g; when the continuum manipulator became longer, its torsional rigidity deteriorated and it failed to lift 50 g.

Enhancement of the torsional rigidity shall be implemented. One possible way is to integrate a passive rigid kinematic chain as reported in [27]. The integrated kinematic chain takes up the space in the center of the manipulator. However, a center lumen is very important for a surgical manipulator to pass through 1) actuation line of grippers or scissors, 2) electrical wires for ablation, 3) rinsing waters, etc. Miniature nickel bellows were then integrated into the dual continuum mechanism to enhance the torsional rigidity of the distal structure, as shown in Fig. 8.

IV. System Descriptions

Implementing the design concepts introduced in Section III, the SURS was designed as shown in Figs. 1 and 2. Three key components are described here in detail.

A. Layout of the Stem Cross Section

The vision unit and the manipulation arms of the SURS are all deployed into the abdomen through a ϕ12-mm skin incision. It is critical to properly utilize the stem's cross-sectional area.

As mentioned in Section III-B and elaborated in Section IV-C, miniature nickel bellows are used to enhance the torsional rigidity without compromising the bending capabilities of the manipulation arms. The standard FC-4 bellows (Servometer LLC.) with a 6.35-mm outer diameter are used. In order to pass two

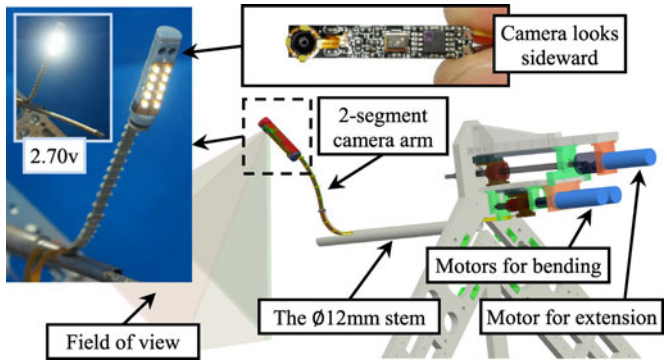

Fig. 6. 3-D vision unit with ten integrated LEDs.

ϕ6.35-mm arms through the ϕ12-mm stem, the two arms have to be deployed one by one.

Using the design concept of the dual continuum mechanism, the guiding cannulae could be bounded into the shape as in the left side of Fig. 5(a). This shape would leave enough space for the other ϕ6.35-mm bellow to pass. With both arms deployed, a 3-mm wide bar could be inserted between the arms to fix both arms in place, as shown in the right side of Fig. 5(a). When one arm is to be pulled out, this bar shall be removed first. This might cause some unintended motions of the other arm.

The upper portion of the cross section is reserved for the vision unit for 1) the continuum camera positioning arm and 2) the flexible PCB strips for LED and camera chips.

B. 3-D Vision Unit

The vision unit shall be folded to form a cylindrical surface to facilitate the insertion through the skin incision as shown in Fig. 1(a). The vision unit could then extend itself and be bent upwards to provide 3-D visualization of the surgical site.

An initial design of the vision unit was presented in [17] but was abandoned here due to the design complexity. An overly complicated vision unit would compromise the overall reliability of the system.

A simpler design was constructed as in Figs. 6 and 7. It consists of 1) the camera head with integrated LEDs, and 2) a two-segment continuum camera positioning arm.

The camera head uses two MO-BL1204LK chips (Misumi Inc.) with a resolution of 640×480. Each chip has a length of 24 mm and a width of 4.5 mm. Two camera chips are placed side by side within the ϕ12-mm camera head, referring to the

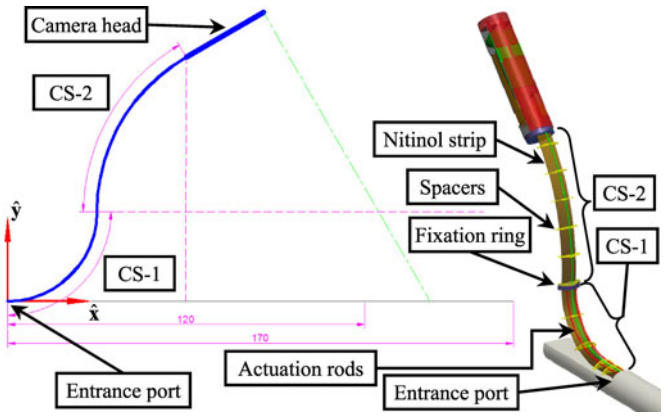

Fig. 7. Two-segment continuum camera positioning arm.

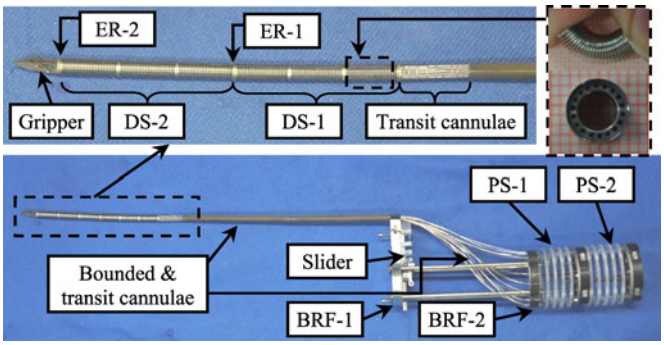

Fig. 8. Exchangeable manipulation arm with a gripper.

camera arrangement as in [16]. The chips' original wires were replaced by flexible PCB strips for easier routing of these wires.

Ten LEDs are attached to the surface of the camera head for illumination. These LEDs are powered at 2.70 V as shown in the inset of Fig. 6. Nominal voltage of these LEDs is 2.95 V. Lighting them at 2.70 V avoids the heating problem. The steady status temperature is about 33 °C when the camera head is placed in an indoor environment under a room temperature of 20 °C with no active ventilation.

A two-segment continuum arm is used to position and orient the camera head. As in Fig. 7, the arm consists of a nitinol strip, a fixation ring, spacers, and thin rods for actuation. The fixation ring is rigidly attached to the nitinol strip. The portion of the nitinol strip from the fixation ring to the arm entrance port is referred to as Camera Segment 1 (CS-1). Two actuation rods are attached to the fixation ring and can slide in the holes of the spacers. Pulling the actuation rods would bend the CS-1 upwards. The portion of the nitinol strip between the camera head and CS-1 is referred to as Camera Segment 2 (CS-2). Another actuation rod is attached to the camera head and can slide in the holes of the spacers. Pushing this rod, which is routed through the CS-1, would bend the CS-2 downwards.

There are 3-DoFs for the camera positioning arm: 2-DoFs for bending and 1-DoF for the translational feed of the CS-1. Their actuation rods are driven by the motorized ball screws in Fig. 6.

Bent shapes of the CS-1 and the CS-2 are assumed to be circular according to the previous studies [28]–[30]. Using this assumption, their dimensions were determined via dimensional synthesis. The preferred viewing range is 120–170 mm from the arm entrance as in Fig. 7. When the CS-1 is assumed for a 90° bending, the lengths of the CS-1 and the CS-2 can be determined as 40, and 60 mm, respectively.

The vision unit is attached to the main structure of the SURS. This might be a problem for its sterilization. A vision unit that can be disassembled should be considered in the future.

C. Exchangeable Manipulation Arms With Gripper

The manipulation arms could largely determine the system's capabilities. The topology of the SURS's arms was carefully selected in order to not only achieve the design compactness but also ensure satisfactory kinematic performance.

According to the comparison of the kinematic performances of various continuum manipulators [31], [32], a two-segment 6-DoF structure was determined as in Fig. 8 since it could better allow a surgeon to orient the end effector (e.g., the gripper). Such a 6-DoF structure also avoids the complex coordination between the bending segments and the parallelogram linkage of the manipulators as in the IREP robot [9], [10].

Design of the SURS's manipulation arm implements the dual continuum mechanism concept from Section III-A. As in Fig. 8, the manipulation arm possesses a gripper, the guiding cannulae and several segments: the DS-2, the DS-1, the PS-1, and the PS-2. The manipulation arm does not include a distal rotary wrist. The reasons mainly include the following three points.

1) The 2-N payload capability of the SURS is expected. A weak distal wrist would compromise the overall payload capability even if the arms are strong enough. Due to the lack of an effective way to provide powerful actuation to the distal wrist, the wrist was, hence, excluded from the design.
2) A distal rotary wrist could provide substantial help while driving a circular suture to penetrate a chunk of tissues. As shown in [24] and [33], a precurved nitinol suture could also be used to facilitate the tissue penetration motion. Without using a distal rotary wrist, such a suture could be pushed out and penetrate the tissues following a circular path, passing the suture threads through the tissues for knot tying.
3) The 6-DoF manipulation arm could position its end effector (the gripper) fairly freely within the translational workspace. Even when a conventional suture has to be used, it is still possible to drive the suture in an incremental manner without using a distal rotary wrist: grip the suture at the midpoint, drive the suture in the desired direction, release the suture and regrip at a point closer to the suture eyelet for the next incremental penetration, repeat till the suture was through.

With these reasons, it was considered the manipulation arm without a distal rotary wrist could still provide the desired functions. Hence, the design was then materialized as in Fig. 8.

The DS-1 and the DS-2 are similar. Each segment consists of three serially connected FC-4 nickel bellows (Servometer LLC.). The bellow has an outer diameter of 6.35 mm and a free

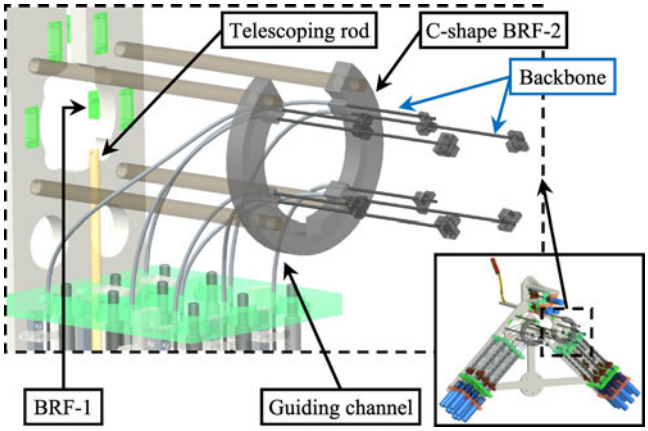

Fig. 9. Actuation assembly of the manipulation arms.

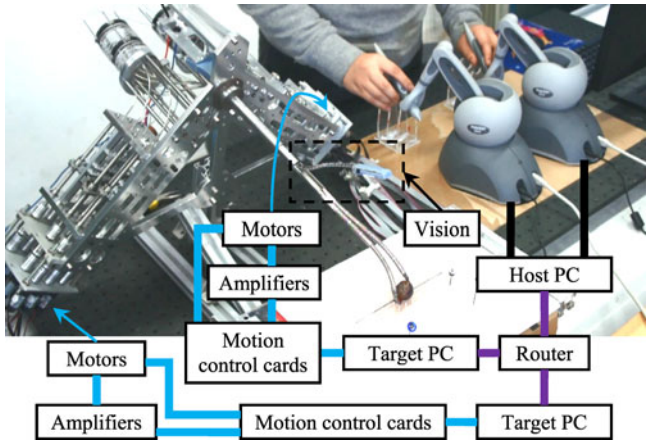

Fig. 10. Control infrastructure of the SURS robot.

length of 18.8 mm. The bellow can be easily bent, compressed, and stretched. After testing, it was found the bellow could undergo a 5.2-mm compression and a 5.0-mm stretching for 10^5 times without developing any visible cracks. Eighteen ϕ0.5-mm through holes were drilled in the convolutions of the bellows by wire electrical discharge machining (EDM) as shown in the inset of Fig. 8.

Nine ϕ0.40-mm nitinol rods as the backbones of the DS-1 are attached to the bellow end marked by End Ring 1 (ER-1), routed through the DS-1, the guiding cannulae, the PS-1, and attached to the end ring of the PS-1. Nine additional ϕ0.40-mm nitinol rods as the backbones of the DS-2 are attached to the bellow end marked by ER-2, routed through the DS-2, the DS-1, the guiding cannulae, the PS-1, and the PS-2, and attached to the PS-2's end ring.

Both the DS-1 and the DS-2 have 3-DoFs: a 2-DoF bending and a 1-DoF extension/compression. These DoFs are actuated by the corresponding motions of the PS-1 and the PS-2.

The guiding cannulae are tightly bounded and the bounded arrangement can be seen from the left portion of Fig. 5(a). As in Fig. 8, transit arrangements of the cannulae are also needed to ensure the cannulae's smoothness.

From the CAD drawing in Fig. 5, there are 20 channels in the bounded cannulae. Eighteen of them are for the backbones of the two segments. The 19th is reserved for the actuation line of the gripper. This actuation line is routed to the slider as shown in Fig. 8. The slider will be pushed and pulled by a telescoping rod in the actuation assembly. The 20th can be used for precurved nitinol suture as proposed in [24] and [33].

The actuation assembly is shown in Fig. 9. After one arm is inserted, two retaining pins can be inserted at the BRF-1 and the BRF-2 (Base Ring Fixtures 1 and 2) positions as in Figs. 8 and 9 to fix the arm to the SURS. The matching BRF-2 in Fig. 9 is a C shape to let the BRF-1 and the cannulae of the arm pass during the arm insertion. After the arm is inserted and fixed, the telescoping rod in Fig. 9 would be connected to the slider in Fig. 8 such that a motorized ball screw drives the gripper.

Eight backbones shown in Fig. 9 would be connected to the end rings of the PS-1 and the PS-2. The eight backbones would be pushed and/or pulled to bend and/or extend/shorten the PS-1 and the PS-2 so as to drive the DS-1 and the DS-2. The eight backbones are actuated by the eight motorized ball screws through the guiding channels as shown in Fig. 9.

An arm with a different gripper could be exchanged during surgery. Since the arm only consists of mechanical components, it can be sterilized by emerging the arm in a liquid agent such as glutaraldehyde and orthophthalaldehyde.

D. Control Infrastructure

The SURS's control infrastructure adopts a conventional setup for teleoperation.

As shown in Fig. 10, two Phantom Omni devices (Sensable Inc.) were connected to a Host PC via IEEE 1394 firewires. They were used for control inputs. The Host PC has a Windows operating system (OS) and it runs a program that sends the tip positions and orientations from the two Omni devices to two Target PCs via a router with LAN connections using a User Datagram Protocol every 10 ms.

Each Target PC controls one manipulation arm and it runs a real-time OS generated by the xPC module of MATLAB. The servo loop on the Target PC was chosen to be 1 ms.

Multiple motion control cards, including the PCL727 D/A cards (AdvanTech Inc.) and the CNT32–8M counter cards (Con-Tec Inc.), are used in the Target PC for the control signal outputs and the motor encoder readings. The motors (A-max 22 motors, GP22A gearheads with a gear ratio of 53:1, and MR32 encoders) and the amplifiers (LSC 30/2) are from Maxon Inc.

During each servo loop, the controller generates motor control signals according to the inputs from the Omni devices and the inverse kinematics of the arm. The implemented teleoperation is detailed in Section VI-D.

At this point, the 3-DoF vision unit remains stationary during the teleoperation.

V. Manipulator Kinematics

Based on the kinematic performance comparison of different continuum manipulators in [31] and [32], the manipulation arms were designed as in Section IV-C. The performance would be quantified through the kinematics presented in this section.

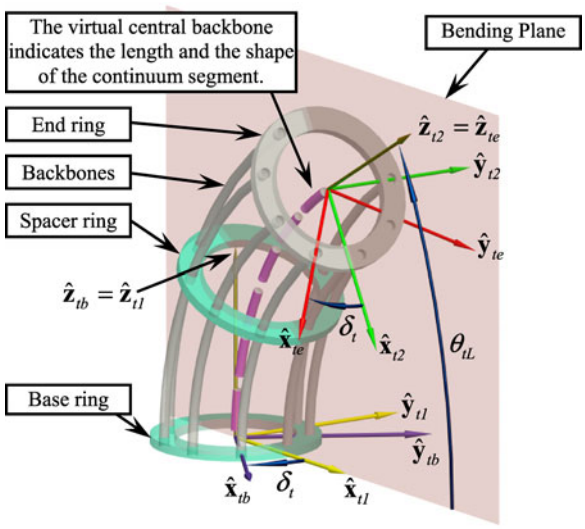

Fig. 11. Nomenclature and coordinates of the *t*th continuum segment.

The manipulation arm utilizes the design concept of the dual continuum mechanism. It consists of several similar continuum segments: the DS-1, the DS-2, the PS-1, and the PS-2. Due to the similarity, Fig. 11 only shows the *t*th segment ($t = 1, 2$) of the distal structure. The kinematics in Section V-C quantifies its kinematic characteristics. Those of the proximal structure and the actuation structure could be obtained similarly.

A. Nomenclature and Coordinate Systems

Nomenclatures are defined in Table I, while four coordinate systems of the *t*th segment are defined as follows.

1) *Base Ring Coordinate* (BRC) $\{tb\} \equiv \{\hat{\mathbf{x}}_{tb}, \hat{\mathbf{y}}_{tb}, \hat{\mathbf{z}}_{tb}\}$ is attached to the base ring of the *t*th segment, whose XY plane coincides with the base ring and its origin is at the ring's center. $\hat{\mathbf{x}}_{tb}$ points from the ring's center to the first backbone, while $\hat{\mathbf{z}}_{tb}$ is perpendicular to the base ring. The backbones are numbered according to the definition of δ_{ti}.
2) *Bending Plane Coordinate 1* is designated as $\{t1\} \equiv \{\hat{\mathbf{x}}_{t1}, \hat{\mathbf{y}}_{t1}, \hat{\mathbf{z}}_{t1}\}$, which shares its origin with $\{tb\}$ and has the continuum segment bending in its *XZ* plane.
3) *Bending Plane Coordinate 2* is designated as $\{t2\} \equiv \{\hat{\mathbf{x}}_{t2}, \hat{\mathbf{y}}_{t2}, \hat{\mathbf{z}}_{t2}\}$ obtained from $\{t1\}$ by a rotation about $\hat{\mathbf{y}}_{t1}$ such that $\hat{\mathbf{z}}_{t1}$ becomes backbone tangent at the end ring. Origin of $\{t2\}$ is at center of the end ring.
4) *End Ring Coordinate* (ERC) $\{te\} \equiv \{\hat{\mathbf{x}}_{te}, \hat{\mathbf{y}}_{te}, \hat{\mathbf{z}}_{te}\}$ is fixed to the end ring of the *t*th segment. $\hat{\mathbf{x}}_{te}$ points from the ring's center to the first backbone and $\hat{\mathbf{z}}_{te}$ is normal to the ring. $\{te\}$ is obtained from $\{t2\}$ by a rotation about $\hat{\mathbf{z}}_{t2}$.

When the second segment is stacked on top of the first segment, $\{1e\}$ coincides with $\{2b\}$.

B. Kinematics of One Segment

The virtual central backbone characterizes the length and the shape of one segment. The kinematics assumes a circular shape for the segments. This assumption was widely adopted [28]–[30] and experimentally verified [27], [29]. The kinematics was derived with sufficient details as in [31] and [32] extending previous results from [28]. The kinematics is briefly summarized here for the completeness.

TABLE II
NOMENCLATURE USED IN KINEMATICS MODELING

Symbol	Representation
i	Index of the backbones, $i = 1, 2, \ldots, m$
t	Index of the segments $t = 1, 2$; numbering of the segments always precedes that of the backbones.
r_{ti}	Distance from the virtual central backbone to the *i*th backbone in the *t*th segment.
β_{ti}	β_{ti} characterizes the division angle from the *i*th backbone to the 1st backbone in the *t*th segment. $\beta_{t1} \equiv 0$ and β_{ti} remain constant once the manipulation arm is built.
L_t, L_{ti}	Length of the central and the *i*th backbone for the *t*th segment.
$\theta_t\,(s)$	The angle of the tangent to the central backbone in the bending plane for the *t*th segment. $\theta_t\,(L_t)$ and $\theta_t\,(0)$ are designated by θ_{tL} and θ_0. $\theta_0 = \pi/2$ is a constant.
$\bar{\theta}_{tL}$	$\bar{\theta}_{tL} \equiv \pi/2 - \theta_{tL}$. Due the definition of θ_{tL}, $\theta_{tL} = 0$ represents a 90° bending. $\bar{\theta}_{tL}$ provides a more intuitive bending quantification.
δ_{ti}	For the *t*th segment, a right-handed rotation angle from $\hat{\mathbf{x}}_{t1}$ about $\hat{\mathbf{z}}_{t1}$ to a ray passing through the central and the *i*th backbones.
δ_t	$\delta_t \equiv \delta_{t1}$ and $\delta_{ti} = \delta_t + (i-1)\beta$
$\boldsymbol{\psi}_t$	$\boldsymbol{\psi}_t = [\,\theta_{tL}\ \ \delta_t\ \ L_t\,]^T$ is a configuration vector which defines the pose of the *t*th segment.
${}^1\mathbf{R}_2$	Coordinate transformation matrix frame *2* to frame *1*.
${}^{tb}\mathbf{p}_t\,(s)$	Position vector of a point along the primary backbone in $\{tb\}$. ${}^{tb}\mathbf{p}_t\,(L_t)$ is the tip position designated by ${}^{tb}\mathbf{p}_{tL}$.

Shape of the *t*th continuum segment can be characterized by $\boldsymbol{\psi}_t = [\,\theta_{tL}\ \ \delta_t\ \ L_t\,]^T$ as defined in Table II.

Tip position of the *t*th segment can be derived as

$$ {}^{tb}\mathbf{p}_{tL} = \frac{L_t}{\theta_{tL} - \theta_0} \begin{bmatrix} \cos\delta_t(\sin\theta_{tL} - 1) \\ \sin\delta_t(1 - \sin\theta_{tL}) \\ -\cos\theta_{tL} \end{bmatrix} \tag{1} $$

where ${}^{tb}\mathbf{p}_{tL} = \begin{bmatrix} 0 & 0 & L_t \end{bmatrix}^T$ when $\theta_{tL} = \theta_0 = \pi/2$.

Rotation matrix ${}^{tb}\mathbf{R}_{te}$ associates $\{te\}$ and $\{tb\}$ as

$$ {}^{tb}\mathbf{R}_{te} = R(\hat{\mathbf{z}}_{tb}, -\delta_t) R(\hat{\mathbf{y}}_{t1}, \theta_0 - \theta_{tL}) R(\hat{\mathbf{z}}_{t2}, \delta_t) \tag{2} $$

where $R(\hat{\mathbf{n}}, \gamma)$ designates a rotation about $\hat{\mathbf{n}}$ by an angle γ.

The instantaneous kinematics is then given by

$$ \dot{\mathbf{x}}_t = \mathbf{J}_{t\boldsymbol{x}\boldsymbol{\psi}} \dot{\boldsymbol{\psi}}_t \quad \text{where} \quad \mathbf{J}_{t\boldsymbol{x}\boldsymbol{\psi}} = \begin{bmatrix} \mathbf{J}_{t\mathbf{v}} \\ \mathbf{J}_{t\boldsymbol{\omega}} \end{bmatrix} \tag{3} $$

$$ \mathbf{J}_{t\boldsymbol{v}} = \begin{bmatrix} L_t \mathrm{c}_{\delta_t} \frac{(\theta_{tL} - \theta_0)\mathrm{c}_{\theta_{tL}} - \mathrm{s}_{\theta_{tL}} + 1}{(\theta_{tL} - \theta_0)^2} & -L_t \frac{\mathrm{s}_{\delta_t}(\mathrm{s}_{\theta_{tL}} - 1)}{\theta_{tL} - \theta_0} & \frac{\mathrm{c}_{\delta_t}(\mathrm{s}_{\theta_{tL}} - 1)}{\theta_{tL} - \theta_0} \\ -L_t \mathrm{s}_{\delta_t} \frac{(\theta_{tL} - \theta_0)\mathrm{c}_{\theta_{tL}} - \mathrm{s}_{\theta_{tL}} + 1}{(\theta_{tL} - \theta_0)^2} & -L_t \frac{\mathrm{c}_{\delta_t}(\mathrm{s}_{\theta_{tL}} - 1)}{\theta_{tL} - \theta_0} & \frac{\mathrm{s}_{\delta_t}(1 - \mathrm{s}_{\theta_{tL}})}{\theta_{tL} - \theta_0} \\ L_t \frac{(\theta_{tL} - \theta_0)\mathrm{s}_{\theta_{tL}} + \mathrm{c}_{\theta_{tL}}}{(\theta_{tL} - \theta_0)^2} & 0 & \frac{-\mathrm{c}_{\theta_{tL}}}{\theta_{tL} - \theta_0} \end{bmatrix} $$

$$ \mathbf{J}_{t\boldsymbol{\omega}} = \begin{bmatrix} -\mathrm{s}_{\delta_t} & \mathrm{c}_{\delta_t}\mathrm{c}_{\theta_{tL}} & 0 \\ -\mathrm{c}_{\delta_t} & -\mathrm{s}_{\delta_t}\mathrm{c}_{\theta_{tL}} & 0 \\ 0 & -1 + \mathrm{s}_{\theta_{tL}} & 0 \end{bmatrix}. \tag{4} $$

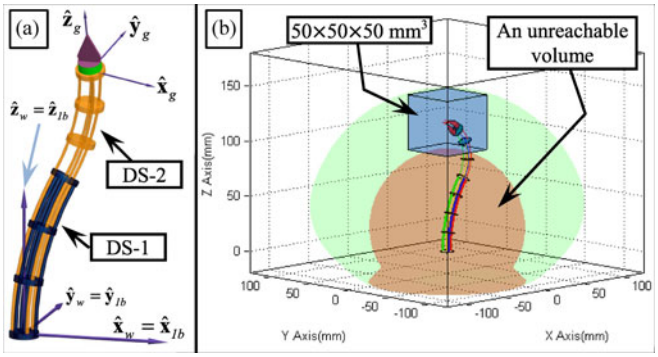

Fig. 12. (a) Coordinates and (b) workspace of the manipulation arm.

TABLE III
STRUCTURE PARAMETERS OF THE MANIPULATION ARM

$\theta_{tL} \in [0, \pi/2]$	$\delta_t \in [-\pi, \pi]$	$r_{ti} = 2.5\,\text{mm}$
$L_t \in [45\,\text{mm}, 65\,\text{mm}]$	${}^g\mathbf{p}_g = [\,0\;\;0\;\;15\,\text{mm}\,]^T$	

C. Kinematics of the Manipulation Arm

The DS-2 is stacked on top of the DS-1 to form the manipulation arm. This configuration was determined based on a comparison of kinematic performances as in [31] and [32]. The coordinates could be assigned as in Fig. 12(a). A configuration vector $\boldsymbol{\xi} = [\,\boldsymbol{\psi}_2^T \;\; \boldsymbol{\psi}_1^T\,]^T$ parameterizes the arm. Kinematics of the tth segment is used to assemble the kinematics of the arm.

Tip position of the gripper in $\{w\}$ and the Jacobian matrix can be written as follows:

$${}^w\mathbf{p}_g = {}^{1b}\mathbf{p}_{1L} + {}^{1b}\mathbf{R}_{2b}\left({}^{2b}\mathbf{p}_{2L} + {}^{2b}\mathbf{R}_{2e}\,{}^{2e}\mathbf{R}_g^g\mathbf{p}_g\right) \tag{5}$$

where ${}^{1b}\mathbf{p}_{1L}$ and ${}^{2b}\mathbf{p}_{2L}$ can be obtained from (1); and ${}^g\mathbf{p}_g$ is the gripper tip position in $\{g\}$.

$$\dot{\mathbf{x}} = \mathbf{J}_{\boldsymbol{x}\xi}\dot{\boldsymbol{\xi}} \tag{6}$$

$$\mathbf{J}_{\mathrm{x}\xi} = \begin{bmatrix} {}^{1b}\mathbf{R}_{2b}(\mathbf{J}_{2\mathbf{v}} - [{}^{2b}\mathbf{R}_g\,{}^g\mathbf{p}_g]^\times\mathbf{J}_{2\boldsymbol{\omega}}) & \mathbf{T}_{C1} \\ {}^{1b}\mathbf{R}_{2b}\mathbf{J}_{2\boldsymbol{\omega}} & \mathbf{J}_{1\boldsymbol{\omega}} \end{bmatrix}. \tag{7}$$

where $\mathbf{T}_{C1} = \mathbf{J}_{1\mathbf{v}} - \left[{}^{1b}\mathbf{R}_{2b}\,{}^{2b}\mathbf{p}_{2L} + {}^{1b}\mathbf{R}_g^g\mathbf{p}_g\right]^\times\mathbf{J}_{1\boldsymbol{\omega}}$, $[\mathbf{p}]^\times$ is the skew-symmetric matrix of a vector $\mathbf{p}$. Expressions of $\mathbf{J}_{1\mathbf{v}}$, $\mathbf{J}_{1\boldsymbol{\omega}}$, $\mathbf{J}_{2\mathbf{v}}$, and $\mathbf{J}_{2\boldsymbol{\omega}}$are from (4).

From the description of the manipulation arm from Section IV-C, the structural parameters of the manipulation arm are summarized in Table III.

Using the parameters, workspace of the manipulation arm could be generated by scanning the arm's configuration space and visualized as in Fig. 12(b). The workspace envelopes a cubic volume of $50\ \text{mm} \times 50\ \text{mm} \times 50\ \text{mm}$, which is enough for a typical cholecystectomy according to [9].

D. Actuation Kinematics

When the DS-1 is bent to a specific configuration $\boldsymbol{\psi}_1$, the desired lengths of the backbones are specified as follows. The detailed derivation could be found in [24].

$$L_{1i} = L_1 + r_{1i}\cos\delta_{1i}(\theta_{1L} - \theta_0). \tag{8}$$

Since the backbones of the DS-2 are routed through the DS-1, there exists an actuation coupling between the two segments. When the DS-1 is actuated, the DS-2's backbones shall be actuated accordingly in order to keep the DS-2's configuration $\boldsymbol{\psi}_2$ unchanged. Hence, the DS-2's backbones should be pushed or pulled according to the following equation:

$$\begin{aligned} L_{2i} = \;& L_1 + r_{2i}\cos(\delta_1 + \beta_{2i})(\theta_{1L} - \theta_0) + L_2 \\ & + r_{2i}\cos\delta_{2i}(\theta_{2L} - \theta_0). \end{aligned} \tag{9}$$

Please note that r_{2i} and β_{2i} also indicate at which positions the DS-2's backbones are routed through the cross section of the DS-1. The first two items in the right side of (9) indicate the backbone length changes due to the DS-1's shape change.

According to the description and its actuation scheme of the dual continuum mechanism in Section III-A, the PS-1 and the PS-2 have their backbones arranged at a bigger radius. The r_{ti} value of the PS-1 and the PS-2 is ten times of that of the DS-1 and DS-2. When an actuation is needed to bend the DS-1 to a specific configuration $\boldsymbol{\psi}_1$, the PS-1 shall be bent to a configuration as follows:

$$\begin{cases} \delta_{\mathrm{PS}-ti} = \delta_{\mathrm{DS}-ti} + \pi \\ \bar{\theta}_{\mathrm{PS}-tL} = 0.1\bar{\theta}_{\mathrm{DS}-tL} \end{cases},\ t = 1, 2 \tag{10}$$

where the δ and $\bar{\theta}$ with different subscripts designate the symbols for the DS and the PS segments. The symbols are defined in Table II.

The PS-1 and the PS-2 are assembled into the AS-1 and AS-2 for actuation. Hence, the configurations of the AS-1 and the AS-2 will be identical to those of the PS-1 and the PS-2. In order to actuate the DS-1 and the DS-2 to the desired configuration $\boldsymbol{\psi}_1$ and $\boldsymbol{\psi}_2$, the AS-1 and the AS-2 should be actuated to the configurations, which could be obtained according to (10). The actuation lengths of the backbones in the AS-1 and the AS-2 could be calculated according (8) and (9), since the AS-1 and the AS-2 are structurally similar to the DS-1 and DS-2.

VI. EXPERIMENTAL CHARACTERIZATIONS

Various experiments were carried out on the SURS to characterize its specifications and demonstrate its capabilities.

A. Deployment

As mentioned previously, the SURS can be folded into a ϕ12-mm cylindrical form, as shown in Fig. 13(a), for insertion into the abdomen. The deployment is shown in Fig. 13.

After insertion, the vision unit extends itself and bends upwards to generate space for the insertion of the manipulation arms, as in Fig. 13(b) and (c). After the camera arm is bent to a desired configuration, a manipulation arm could be inserted as in Fig. 13(d). After the first arm is fully inserted, enough space would be generated within the ϕ12-mm stem, the second arm could be inserted as in Fig. 13(e). The two arms could then perform surgical tasks as in Fig. 13(f). It should be noted that

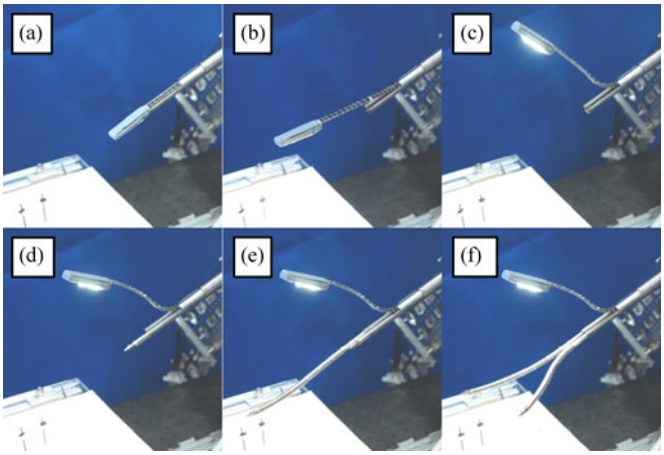

Fig. 13. Deployment of the SURS robot.

either arm could be pulled out and exchanged during a surgery. They just cannot be pulled out or inserted together.

Each segment in the manipulation arms and the camera arm can bend 90° within 2 s. Theoretically the deployment could be completed within half a minute. Due to the limited manufacturing accuracy and the tight tolerances between various system components, forward feeding of the camera arm and insertion of the manipulation arms are not always smooth. The deployment is often prolonged to 2–5 min.

B. Actuation Compensation of the Manipulation Arms

There often exists a shape discrepancy between the actual shape and the assumed ideal shape of one segment [34], [35]. Actuation compensation is needed to deform the manipulation arm into the desired shapes to enable teleoperation.

The compensation was conducted as follows. Each segment (DS-1 and DS-2) of the two manipulation arms was driven to a desired configuration that was specified by ψ_t. An optical tracker (Micron Tracker SX60, Claron Technology Inc.) was used to identify the actual bent configuration of each segment. Based on the bending discrepancy, an actuation compensation algorithm was implemented to correct the bending discrepancy. Instead of using the tracker, incorporating shape sensing could also be considered for this compensation process.

The Micron tracker tracked a marker that was attached to the segment when the segment was bent to different ψ_t values. In this process, the marker's orientation would change and this might affect the tracker's tracking accuracy. Hence, a set of experiments were first carried out to verify the tracker's accuracy under this specific setting. As shown in Fig. 14(a), a customized part was attached to a rotary stage. Three markers are attached to this part. The part was rotated for 360°, mimicking the calibration process of changing the δ_t from 0° to 360°. The tracked marker positions were used to calculate the tip's orientation with respect to the base and the result was compared to the tip's actual known orientation. It was shown that 40-mm long markers should be used and the tracker should be placed at four different positions to keep the orientation tracking errors within ±0.5°.

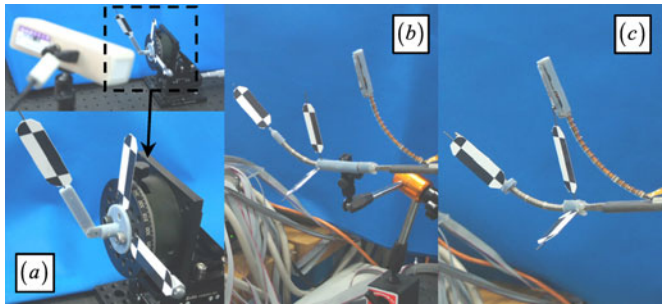

Fig. 14. Experimental setups for the bending calibration: (a) tracking accuracy verification, (b) DS-2's calibration, (c) DS-1's calibration.

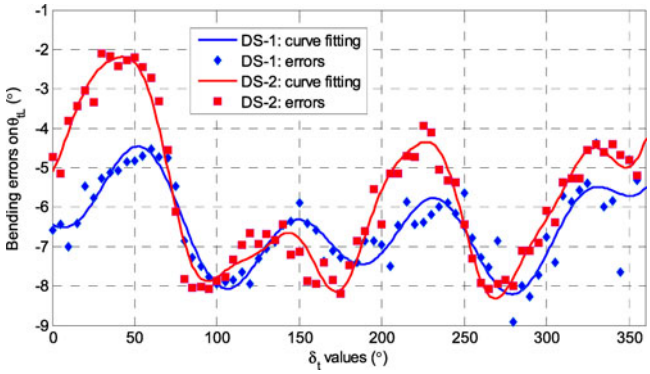

Fig. 15. Bending errors of the DS-2 and the DS-1 of the left arm before compensation.

TABLE IV
ACTUATION COMPENSATION COEFFICIENTS OF THE CS-1 AND THE CS-2

$a_{21} = 6.768$	$a_{22} = 14.42$	$a_{23} = 1.302$	$a_{24} = 15.63$	$a_{25} = 0.270$
$b_{21} = 0.293$	$b_{22} = 1.778$	$b_{23} = 4.013$	$b_{24} = 1.813$	$b_{25} = 8.001$
$c_{21} = -2.485$	$c_{22} = -1.865$	$c_{23} = -1.553$	$c_{24} = 1.148$	$c_{25} = -0.610$
$a_{11} = 41.70$	$a_{12} = 51.26$	$a_{13} = 1.064$	$a_{14} = 21.53$	$a_{15} = 0.337$
$b_{11} = 0.3724$	$b_{12} = 0.650$	$b_{13} = 3.994$	$b_{14} = 0.872$	$b_{15} = 2.998$
$c_{11} = -1.365$	$c_{12} = 1.123$	$c_{13} = -2.266$	$c_{14} = 3.657$	$c_{15} = -2.151$

These results provided a guideline on how to accurately track the tip orientation of each segment.

Tip orientations of the DS-2 were measured while setting θ_{2L}, δ_2, and L_2 to various values. As in Fig. 14(b), a tube was used to constrain the DS-1. Two markers formed the base frame, whereas the third marker was attached to the gripper to indicate the tip orientation. Fig. 15 shows the bending errors on θ_{2L} of the DS-2 of the left arm when δ_2 was commanded between 0° and 360° with θ_{2L} commanded at 45° and L_2 commanded at 55 mm. These errors were fitted using the following function:

$$e_{tL} = \sum_{k=1}^{5} [a_{tk} \sin(b_{tk}\delta_t + c_{tk})],\ t = 1 \text{ or } 2. \qquad (11)$$

The coefficients a_{tk}, b_{tk}, and c_{tk} are listed in Table IV. Then, the actuation compensation for the DS-2 could be expressed as

$$\tilde{\theta}_{tL} = \theta_{tL} + \frac{\theta_{tL} - \pi/2}{\pi/4} e_{tL} \frac{\pi}{180^\circ},\ t = 1 \text{ or } 2. \qquad (12)$$

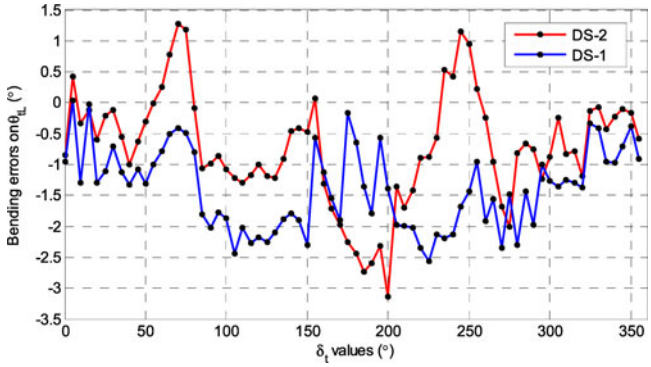

Fig. 16. Bending errors of the DS-2 and the DS-1 of the left arm after compensation

where $\tilde{\theta}_{tL}$ is the commanded value for a desired θ_{tL} bending. e_{tL} has a unit of degree and it shall be converted into radian.

Due to redundant arrangement of the backbones in the DS-2, the errors on δ_2 were between $\pm 1.5°$, which was considered acceptable without actuation compensation. It was also found that changing the L_2 value did not noticeably affect the bending errors on θ_{2L} or δ_2. This might be due to the tight distribution of the bellow convolutions. When L_2 was varied, the convolutions were evenly compressed or stretched.

Bending of the DS-1 was calibrated similarly as shown in Fig. 14(c). Two markers were attached to its base to form the base frame. The third marker was attached to the end ring of the DS-1 to indicate the tip orientation.

The bending errors on θ_{1L} of the DS-1 of the left arm were plotted in Fig. 15, when δ_1 was commanded between 0° and 360° with θ_{1L} commanded at 45° and L_1 commanded at 55 mm. These errors were fitted using the same function as in (11) with the coefficients listed in Table IV for $t = 1$ and $k = 1, 2, \ldots, 5$. The actuation compensation can be implemented using (12) with the corresponding coefficients substituted.

Using the compensated command values $\tilde{\theta}_{tL}(t = 1, 2)$, the bending discrepancy was reduced. As shown in Fig. 16, the average bending errors on θ_{tL} of the DS-1 and DS-2 are $-1.39°$ and $-0.72°$, respectively, for the left arm.

Actuation compensation of the DS-1 and the DS-2 of the right arm could be implemented in a similar manner.

The actuation compensation was then incorporated into the teleoperation of the manipulation arms as in Section VI-D.

C. Payload Tests

The manipulation arms consist of continuum structures. The inherent flexibility could lead to compliant safe interactions with patient tissues. On the other hand, the arms should also possess reasonable payload capabilities to enable manipulation tasks. A set of weight-lifting experiments were then carried out to quantify the payload capabilities of the arms.

As shown in Fig. 17(a), an arm was commanded to four representative configurations as illustrated in Fig. 17(c).

1) $[\theta_{1L}\ \delta_1\ L_1\ \theta_{2L}\ \delta_2\ L_2]^T = [\pi/2\ 0\ 55\,\text{mm}\ \pi/2\ 0\ 55\,\text{mm}]^T$.

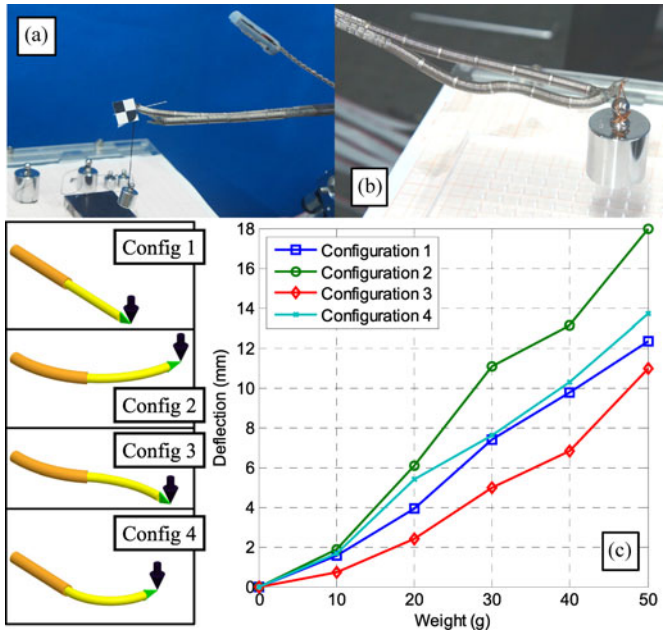

Fig. 17. Payload tests of the manipulation arms: (a) small weights, (b) extreme condition, and (c) deflections caused by the small weights.

2) $[\theta_{1L}\ \delta_1\ L_1\ \theta_{2L}\ \delta_2\ L_2]^T = [\pi/4\ 0\ 55\,\text{mm}\ \pi/4\ 0\ 55\,\text{mm}]^T$.
3) $[\theta_{1L}\ \delta_1\ L_1\ \theta_{2L}\ \delta_2\ L_2]^T = [\pi/4\ 0\ 55\,\text{mm}\ \pi/4\ \pi\ 55\,\text{mm}]^T$.
4) $[\theta_{1L}\ \delta_1\ L_1\ \theta_{2L}\ \delta_2\ L_2]^T = [\pi/2\ 0\ 55\,\text{mm}\ 0\ 0\ 55\,\text{mm}]^T$.

Different weights (10 g to 50 g in increments of 10 g) were hung to the gripper. The deflections were measured using the tracker with a point marker, and the deflections are plotted in Fig. 17(c).

It can be observed that when these small weights were applied to the gripper, the arm underwent small deflections. These deflections (10 mm $\sim$ 18 mm) are considered small compared to the overall length of the manipulation arm (around 150 mm). Due to the presence of a human operator in the teleoperation with 3-D visual guidance, these small deflections could be knowingly corrected by the user inputs.

On the other hand, the 150-mm long manipulation arm is strong enough to lift a 200-g weight as shown in Fig. 17(b). The arm was severely deflected. A more advanced elasticity model will be needed to allow the arm to handle these heavy weights precisely. Without such a model, the arm could still be useful in the scenarios where high payload capability and low positioning accuracy is needed (e.g., tightening a knot).

It might be different from one to another on how much weight and deflection one can properly handle based on his/her familiarity of the system and the sense of the arm's elasticity.

D. Teleoperation

The teleoperation of the SURS adopts a typical setup. Two Omni devices were used for control inputs to drive the two arms. Each Omni devices was registered to the world coordinate $\{w\}$

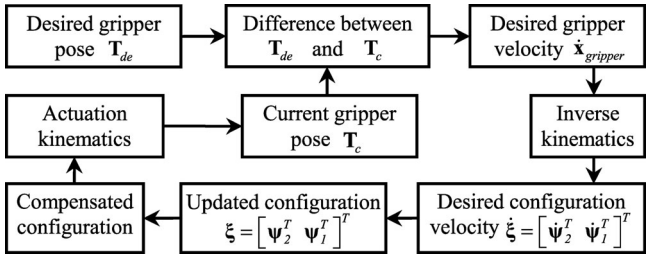

Fig. 18. Teleoperation scheme of one manipulation arm.

(namely the BRC $\{1b\}$ of the DS-1 as in Fig. 12) of the left or the right arm. As in Fig. 18, the position and orientation of one Omni device are sent to one arm's controller to form the desired pose of the gripper (as a homogeneous transformation matrix $\mathbf{T}_{de}$). The difference between the desired gripper pose $\mathbf{T}_{de}$ and the current gripper pose $\mathbf{T}_c$ is used to calculate the desired gripper velocity $\dot{\mathbf{x}}_{\text{gripper}}$. The desired configuration velocity $\dot{\boldsymbol{\xi}} = [\dot{\boldsymbol{\psi}}_2^T \ \dot{\boldsymbol{\psi}}_1^T]^T$ can be obtained through the inverse kinematics using a singularity-robust formulation as in (13). Then, the configuration $\boldsymbol{\xi}$ is updated and a compensated configuration is calculated according to (12). Backbone actuation commands are then issued according to the actuation kinematics in (8) and (9) based on the compensated configuration. In the next servo loop, the current gripper pose $\mathbf{T}_c$ is updated using the direct kinematics and compared again with $\mathbf{T}_{de}$. Currently the servo loop is executed every 1 ms. The inputs from the Omni devices are updated every 10 ms.

$$\dot{\boldsymbol{\xi}} = \begin{cases} \mathbf{J}_{\mathbf{x}\xi}^T(\mathbf{J}_{\mathbf{x}\xi}\mathbf{J}_{\mathbf{x}\xi}^T + \lambda\mathbf{I})^{-1}\dot{\mathbf{x}}, & \sigma_m < \varepsilon \\ \mathbf{J}_{\mathbf{x}\xi}^T(\mathbf{J}_{\mathbf{x}\xi}\mathbf{J}_{\mathbf{x}\xi}^T)^{-1}\dot{\mathbf{x}}, & \text{otherwise} \end{cases} \tag{13}$$

where $\mathbf{J}_{\mathbf{x}\xi}$ is from (7), σ_m is the nonzero smallest singular value, and λ and ε are small positive values (both 0.05 in this implementation).

The SURS was then teleoperated to perform a few representative tasks. Fig. 19 demonstrates the suturing task, which involves repeated tissue penetration and knot tying.

Tissue penetration using a 3/8 circular suture was conducted as shown in Fig. 19(a). However, there existed some tissue tearing during the penetration, which can be identified from the deflected mockup tissue in Fig. 19(a.3). It was originally expected that this tearing could be reduced via incremental penetration. Namely, the arm repeatedly grips, pulls (or pushes), and releases the suture so that the suture could still penetrate the tissue little by little in a circular path even when the arm does not possess a distal rotary wrist. It was shown this motion is quite difficult to realize in practice due to the nonnegligible width of the gripper jaws and unpredictable slipping between the gripper and the suture. Incorporating a distal rotary wrist should be considered for a smooth tissue penetration, if the wrist maintains a high torsional stiffness so that overall payload capability will not be affected.

An anaglyph view from the camera head is shown in Fig. 19(a.4), which is assembled from the images from the two camera chips. The chips were calibrated using existing algorithms. Due to the low imaging quality, an external camera was used to capture the arm motions in Figs. 19 and 20.

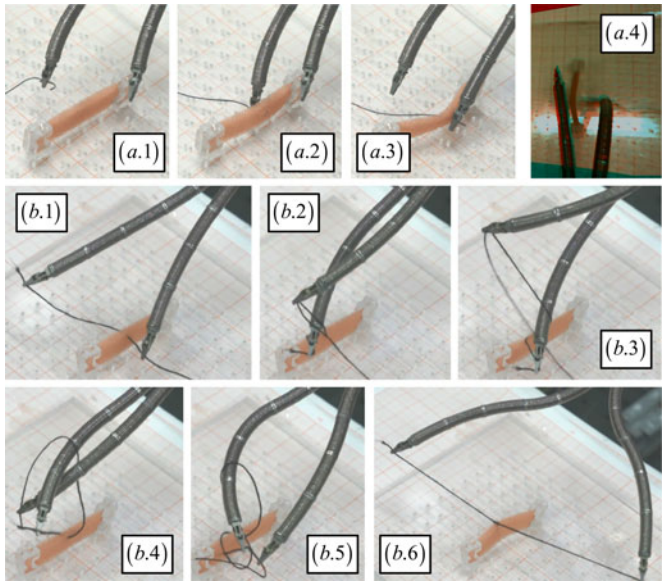

Fig. 19. Suturing task: (a) tissue penetration, and (b) knot tying.

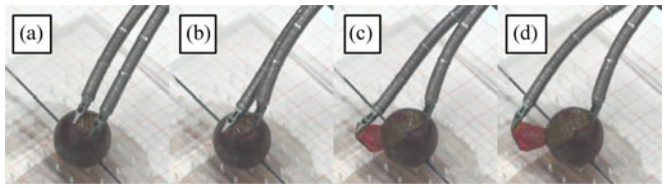

Fig. 20. Grape peeling using the SURS robot.

Knot tying was carried out as follows in Fig. 19(b): (b.1) two ends of one thread were gripped by the two arms; (b.2 and b.3) the left arm wrapped the thread around the right arm; (b.4) the left arm picked the end of the thread from below the right arm; and (b.5 and b.6) the knot was formed and tightened. This newly constructed system was operated by several engineering students and they all can tie a knot within 2 min after training sessions with the system for half a day. More comprehensive experimentation about the learning curve, etc., would be carried out in the future.

The SURS was also teleoperated to peel a grape as in Fig. 20 to demonstrate the delicate motions of the two arms. One arm was used to keep the grape still and the other arm poked into the grape and peeled the skin off the grape successfully.

VII. Conclusion and Future Work

This paper presents the design, construction, kinematics modeling, and experimental characterizations of the SURS for SPL. The SURS robot can be deployed into abdomen through a ϕ12-mm port in its folded configuration and can then be unfolded into a dual-arm configuration for surgical interventions. This development aims at achieving improved system specifications

and pushing the design boundaries of SPL robots for smaller incision ports and enhanced capabilities.

After actuation compensation, the SURS robot can pose its two exchangeable manipulation arms within the workspace with acceptable accuracy: Average bending errors of the structural segments were reduced to $-0.72°$ to $-1.39°$. When the arms are subject to small weights, the deflections are also relatively small and can be knowingly corrected by a user when the arms are teleoperated under the 3-D visual guidance provided by the vision unit. Motion capabilities, such as suturing and grape skin peeling, were demonstrated.

The manipulation arm does not possess a distal rotary wrist due to the lack of effective actuation schemes to maintain high stiffness and generate high output torque. The absence of such a wrist leads to some tissue tearing during tissue penetration in a suturing task. If the tissue tearing shall be avoided, using a precurved nitinol suture or incorporating a rotary wrist has to be considered.

Without such a distal wrist, the SURS still showed satisfactory motion capabilities. Its full potentials could be more completely demonstrated by future developments, such as the integration of more exchangeable surgical tools (e.g., cautery and ablation tools). Then, the SURS could be further gauged in animal studies or even clinical tests.

REFERENCES

[1] P. G. Curcillo, II, A. S. Wu, E. R. Podolsky, C. Graybeal, N. Katkhouda, A. Saenz, R. Dunham, S. Fendley, M. Neff, C. Copper, M. Bessler, A. A. Gumbs, M. Norton, A. Iannelli, R. Mason, A. Moazzez, L. Cohen, A. Mouhlas, and A. Poor, "Single-port-access (SPA™) cholecystectomy: A multi-institutional report of the first 297 cases," *Surgical Endoscopy*, vol. 24, no. 8, pp. 1854–1860, 2010.

[2] Y. Sekiguchi, Y. Kobayashi, Y. Tomono, H. Watanabe, K. Toyoda, K. Konishi, M. Tomikawa, S. Ieiri, K. Tanoue, M. Hashizume, and M. G. Fujie, "Development of a tool manipulator driven by a flexible shaft for single port endoscopic surgery," in *Proc. IEEE/RAS-EMBS Int. Conf. Biomed. Robot. Biomechatronics*, Tokyo, Japan, 2010, pp. 120–125.

[3] Y. Kobayashi, Y. Sekiguchi, T. Noguchi, Y. Takahashi, Q. Liu, S. Oguri, K. Toyoda, M. Uemura, S. Ieiri, M. Tomikawa, T. Ohdaira, M. Hashizume, and M. G. Fujie, "Development of a robotic system with six-degrees-of-freedom robotic tool manipulators for single-port surgery," *Int. J. Med. Robot. Comput. Assisted Surg.*, to be published.

[4] H. Lee, Y. Choi, and B.-J. Yi, "Stackable 4-BAR manipulators for single port access surgery," *IEEE/ASME Trans. Mechatronics*, vol. 17, no. 1, pp. 157–166, Feb. 2012.

[5] H. Samson, "Titan medical inc. completes functional prototype of its single port orifice robotic technology (SPORT(TM)) surgical system," *Marketwired*, Toronto, Canada, 2013.

[6] M. Piccigallo, U. Scarfogliero, C. Quaglia, G. Petroni, P. Valdastri, A. Menciassi, and P. Dario, "Design of a novel bimanual robotic system for single-port laparoscopy," *IEEE/ASME Trans. Mechatronics*, vol. 15, no. 6, pp. 871–878, Dec. 2010.

[7] G. Petroni, M. Niccolini, A. Menciassi, P. Dario, and A. Cuschieri, "A novel intracorporeal assembling robotic system for single-port laparoscopic surgery," *Surgical Endoscopy*, vol. 27, no. 2, pp. 665–670, Feb. 2013.

[8] W.-H. Shin and D.-S. Kwon, "Surgical robot system for single-port surgery with novel joint mechanism," *IEEE Trans. Biomed. Eng.*, vol. 60, no. 4, pp. 937–944, Apr. 2013.

[9] J. Ding, R. E. Goldman, K. Xu, P. K. Allen, D. L. Fowler, and N. Simaan, "Design and coordination kinematics of an insertable robotic effectors platform for single-port access surgery," *IEEE/ASME Trans. Mechatronics*, vol. 18, no. 5, pp. 1612–1624, Oct. 2013.

[10] K. Xu, R. E. Goldman, J. Ding, P. K. Allen, D. L. Fowler, and N. Simaan, "System design of an insertable robotic effector platform for single port access (SPA) surgery," in *Proc. IEEE/RSJ Int. Conf. Intell. Robots Syst.*, St. Louis, MO, USA, 2009, pp. 5546–5552.

[11] G.-P. Haber, M. A. White, R. Autorino, P. F. Escobar, M. D. Kroh, S. Chalikonda, R. Khanna, S. Forest, B. Yang, F. Altunrende, R. J. Stein, and J. H. Kaouk, "Novel robotic da vinci instruments for laparoendoscopic single-site surgery," *Urology*, vol. 76, no. 6, pp. 1279–1282, Dec. 2010.

[12] J. H. Kaouk, G.-P. Haber, R. Autorino, S. Crouzet, A. Ouzzane, V. Flamand, and A. Villers, "A novel robotic system for single-port urologic surgery: First clinical investigation," *Eur. Urol.*, vol. 66, no. 6, pp. 1033–1043, Dec. 2014.

[13] T. Hu, P. K. Allen, N. J. Hogle, and D. L. Fowler, "Insertable surgical imaging device with pan, tilt, zoom, and lighting," in *Proc. IEEE Int. Conf. Robot. Autom.*, Pasadena, CA, USA, 2008, pp. 2948–2953.

[14] B. S. Terry, Z. C. Mills, J. A. Schoen, and M. E. Rentschler, "Single-port-access surgery with a novel magnet camera system," *IEEE Trans. Biomed. Eng.*, vol. 59, no. 4, pp. 1187–1193, Apr. 2012.

[15] C. A. Castro, A. Alqassis, S. Smith, T. Ketterl, Y. Sun, S. Ross, A. Rosemurgy, P. P. Savage, and R. D. Gitlin, "A wireless robot for networked laparoscopy," *IEEE Trans. Biomed. Eng.*, vol. 60, no. 4, pp. 930–936, Apr. 2013.

[16] M. Simi, M. Silvestri, C. Cavallotti, M. Vatteroni, P. Valdastri, A. Menciassi, and P. Dario, "Magnetically activated stereoscopic vision system for laparoendoscopic single-site surgery," *IEEE/ASME Trans. Mechatronics*, vol. 18, no. 3, pp. 1140–1151, Jun. 2013.

[17] K. Xu, J. Zhao, and Z. Dai, "A foldable stereo vision unit for single port access laparoscopy," presented at the *IEEE Int. Conf. Robotics and Automation*, Hong Kong, China, 2014.

[18] S. J. Phee, S. C. Low, Z. L. Sun, K. Y. Ho, W. M. Huang, and Z. M. Thant, "Robotic system for no-scar gastrointestinal surgery," *Int. J. Med. Robot. Comput. Assisted Surg.*, vol. 4, no. 1, pp. 15–22, Mar. 2008.

[19] D. J. Abbott, C. Becke, R. I. Rothstein, and W. J. Peine, "Design of an endoluminal notes robotic system," in *Proc. IEEE/RSJ Int. Conf. Intell. Robots Syst.*, San Diego, CA, USA, 2007, pp. 410–416.

[20] A. C. Lehman, J. Dumpert, N. A. Wood, L. Redden, A. Q. Visty, S. Farritor, B. Varnell, and D. Oleynikov, "Natural orifice cholecystectomy using a miniature robot," *Surgical Endoscopy*, vol. 23, no. 2, pp. 260–266, Feb. 2009.

[21] K. Harada, E. Susilo, A. Menciassi, and P. Dario, "Wireless reconfigurable modules for robotic endoluminal surgery," in *Proc. IEEE Int. Conf. Robot. Autom.*, Kobe, Japan, 2009, pp. 2699–2704.

[22] G. Tortora, M. Salerno, T. Ranzani, S. Tognarelli, P. Dario, and A. Menciassi, "A modular magnetic platform for natural orifice transluminal endoscopic surgery," in *Proc. IEEE Annu. Int. Conf. Eng. Med. Biol. Soc.* Osaka, Japan, 2013, pp. 6265–6268.

[23] G. Tortora, A. Dimitracopoulos, P. Valdastri, A. Menciassi, and P. Dario, "Design of miniature modular *in vivo* robots for dedicated tasks in minimally invasive surgery," in *Proc. IEEE/ASME Int. Conf. Adv. Intell. Mechatronics* Budapest, Hungary, 2011, pp. 327–332.

[24] J. Zhao, X. Zheng, M. Zheng, A. J. Shih, and K. Xu, "An endoscopic continuum testbed for finalizing system characteristics of a surgical robot for notes procedures," in *Proc. IEEE/ASME Int. Conf. Adv. Intell. Mechatronics*, Wollongong, Australia, 2013, pp. 63–70.

[25] C. W. Jeong, S. H. Kim, H. T. Kim, S. J. Jeong, S. K. Hong, S.-S. Byun, and S. E. Lee, "Insufficient joint forces of first-generation articulating instruments for laparoendoscopic single-site surgery," *Surgical Innovation*, vol. 20, no. 5, pp. 466–470, Oct. 2013.

[26] B. A. Jones and I. D. Walker, "Kinematics for multisection continuum robots," *IEEE Trans. Robot. Autom.*, vol. 22, no. 1, pp. 43–55, Feb. 2006.

[27] K. Xu, M. Fu, and J. Zhao, "An experimental kinestatic comparison between continuum manipulators with structural variations," presented at the *IEEE Int. Conf. Robotics and Automation*, Hong Kong, China, 2014.

[28] K. Xu and N. Simaan, "An investigation of the intrinsic force sensing capabilities of continuum robots," *IEEE Trans. Robot.*, vol. 24, no. 3, pp. 576–587, Jun. 2008.

[29] K. Xu and N. Simaan, "Analytic formulation for the kinematics, statics and shape restoration of multibackbone continuum robots via elliptic integrals," *J. Mechanisms Robot.*, vol. 2, no. 011006, pp. 1–13, Feb. 2010.

[30] R. J. Webster and B. A. Jones, "Design and kinematic modeling of constant curvature continuum robots: A review," *Int. J. Robot. Res.*, vol. 29, no. 13, pp. 1661–1683, Nov. 2010.

[31] K. Xu and X. Zheng, "Configuration comparison for surgical robotic systems using a single access port and continuum mechanisms," in *Proc. IEEE Int. Conf. Robot. Autom.*, Saint Paul, MN, USA, 2012, pp. 3367–3374.

[32] K. Xu, J. Zhao, and X. Zheng, "Configuration comparison among kinematically optimized continuum manipulators for robotic surgeries through a single access port," *Robotica*, to be published.
[33] K. Xu, J. Zhao, J. Geiger, A. J. Shih, and M. Zheng, "Design of an endoscopic stitching device for surgical obesity treatment using a N.O.T.E.S approach," in *Proc. IEEE/RSJ Int. Conf. Intell. Robots Syst.*, San Francisco, CA, USA, 2011, pp. 961–966.
[34] K. Xu and N. Simaan, "Actuation compensation for flexible surgical snake-like robots with redundant remote actuation," in *Proc. IEEE Int. Conf. Robot. Autom.*, Orlando, FL, USA, 2006, pp. 4148–4154.
[35] N. Simaan, K. Xu, A. Kapoor, W. Wei, P. Kazanzides, P. Flint, and R. H. Taylor, "Design and integration of a telerobotic system for minimally invasive surgery of the throat," *Int. J. Robot. Res.*, vol. 28, no. 9, pp. 1134–1153, 2009.

Kai Xu (S'06–M'11) received the B.E. and M.S. degrees from the Department of Precision Instruments and Mechanology, Tsinghua University, Beijing, China, in 2001 and 2004, respectively, and the Ph.D. degree (with distinction) from the Department of Mechanical Engineering, Columbia University, New York, NY, USA, in 2009.

Since 2010, he has been with the University of Michigan–Shanghai Jiao Tong University Joint Institute, Shanghai Jiao Tong University, Shanghai, China, where he is currently an Assistant Professor and the Director of the Robotics Innovation and Intervention Laboratory. His research interests include surgical robots, exoskeletons, humanoid robots, prosthetic hands, special industrial robots, and continuum mechanisms.

Jiangran Zhao (S'12) received the B.S. degree from the University of Michigan–Shanghai Jiao Tong University Joint Institute, Shanghai Jiao Tong University, Shanghai, China, in 2011. He is currently working toward the Ph.D. degree in the same institute.

His research interests include surgical robots and continuum mechanisms.

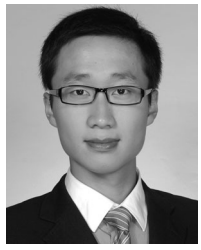

Minxiao Fu received the B.S. degree from the School of Mechanical and Power Engineering, East China University of Science and Technology, Shanghai, China, in 2012. He is currently working toward the M.S. degree in the University of Michigan–Shanghai Jiao Tong University Joint Institute, Shanghai Jiao Tong University, Shanghai.